Volume 54
Number 27
21 July 2025
Pages 10481-10794

Dalton Transactions

An international journal of inorganic chemistry

rsc.li/dalton

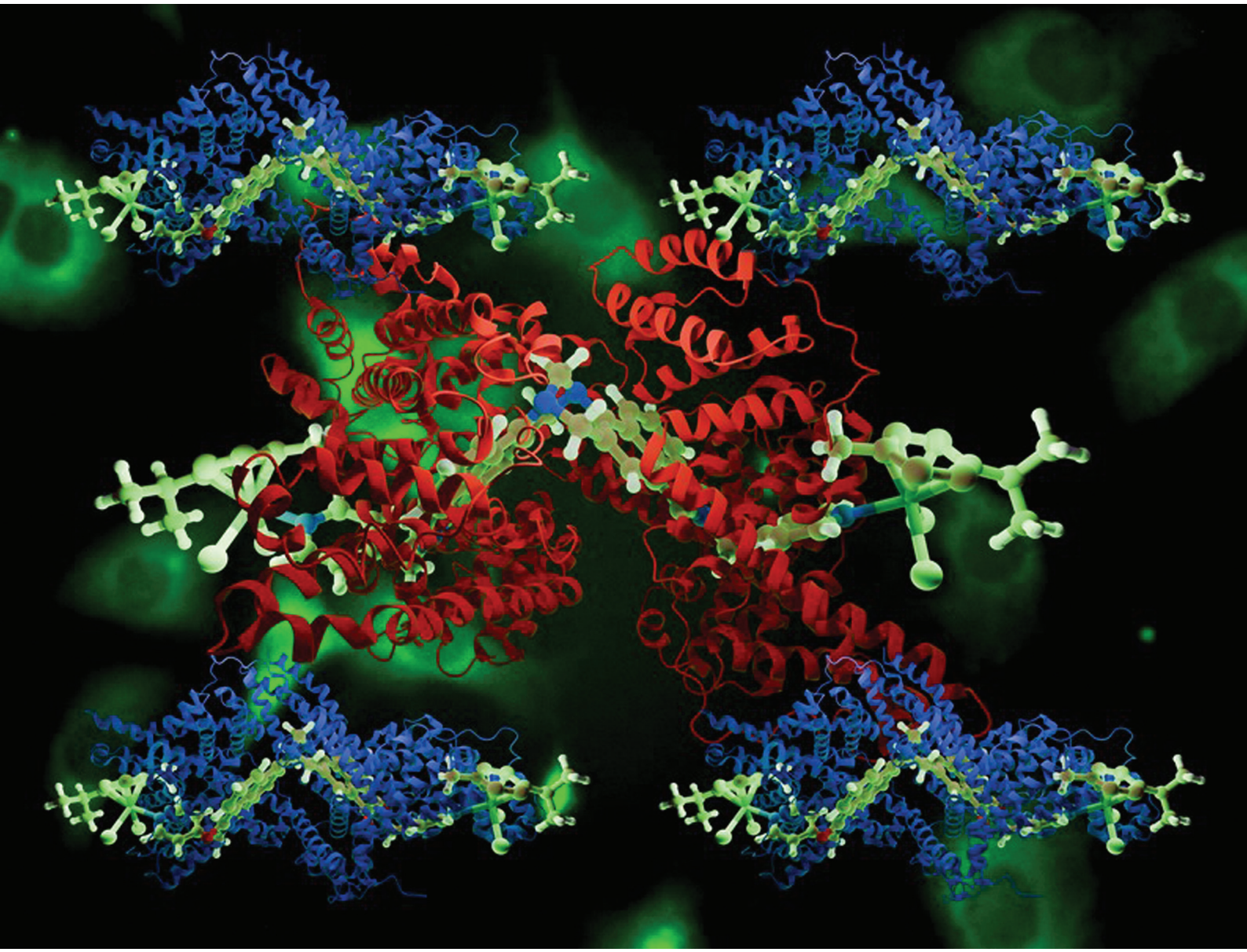

ISSN 1477-9226

ROYAL SOCIETY OF CHEMISTRY

PAPER

Sankarasekaran Shanmugaraju *et al.*
p-Cymene–Ru(II)–organometallic conjugates based on 'V-shaped' 4-amino-1,8-naphthalimide Tröger's base scaffolds: synthesis, photophysics, bioimaging, and BSA/HSA binding studies

Dalton Transactions

ROYAL SOCIETY OF CHEMISTRY

PAPER

View Article Online
View Journal | View Issue

Cite this: *Dalton Trans.*, 2025, **54**, 10549

p-Cymene–Ru(II)–organometallic conjugates based on 'V-shaped' 4-amino-1,8-naphthalimide Tröger's base scaffolds: synthesis, photophysics, bioimaging, and BSA/HSA binding studies†

Binduja Mohan, [a] Anna Jose, [a] Indrajit Bhattacharjee, [b] Raju Saravanan, [a] Mannanthara Kunhumon Noushija, [a] Mintu Porel, [a] Bibhu Ranjan Sarangi [b,c] and Sankarasekaran Shanmugaraju *[a]

Three new *p*-cymene–Ru(II) organometallic conjugates (**TB-Ru-1**, **TB-Ru-2**, and **TB-Ru-3**) have been synthesised in good yield *via* metal–ligand coordination chemistry using three different freshly prepared fluorescent 4-amino-1,8-naphthalimide Tröger's base (TBNap) scaffolds (**TBNap-1**, **TBNap-2**, and **TBNap-3**). Standard spectroscopic techniques characterised the newly designed conjugates, and their molecular structures were obtained through computational optimisations. The photophysical studies of conjugates showed characteristic UV-visible absorption and fluorescence emission peaks. Moreover, the binding ability of conjugates towards Bovine Serum Albumin (BSA) and Human Serum Albumin (HSA) was probed by UV-visible absorption and fluorescence titration studies, which demonstrated substantial binding properties of the conjugates with BSA and HSA, resulting in a significant increase in absorption intensity and fluorescence quenching. The association constant (K_a) and fluorescence quenching constants (K_{SV}) were determined to be 10^4 to 10^5 M^{-1}. Additionally, cellular uptake studies using the 3T3 (embryonic mouse fibroblast) cell line demonstrated rapid internalisation with minimal cytotoxicity, suggesting the potential of these conjugates as bioimaging probes. These results underscore the possible applications of newly designed TBNap-based Ru(II) organometallic conjugates in biomedical fields.

Received 31st March 2025,
Accepted 11th June 2025

DOI: 10.1039/d5dt00769k

rsc.li/dalton

Introduction

Proteins are complex chemical substances that are indispensable for the vitality of life, performing multifaceted roles ranging from transportation and foundational building blocks to even assuming roles as potential pathogens within the realm of biology.[1,2] In the circulatory system, serum albumin (SA) is a predominant extracellular protein, comprising approximately 60% of the plasma protein pool and performing several essential physiological functions.[3,4] SA upholds blood pH (human blood pH = 7.36–7.44) equilibrium and maintains blood colloid osmotic pressure.[5] In addition, proteins play a critical role in facilitating the transport of essential fatty acids, drugs, and other vital metabolites throughout the human body.[6] The capability of SA proteins to act as carriers for numerous drugs enhances mobility within the body. Interestingly, the drug–protein interactions can form a complex that holds significance as a potential storage reservoir for the drug.[7] Among the various serum albumins, bovine serum albumin (BSA) and human serum albumin (HSA) have emerged as the focal point of study as they play an essential role in various metabolic processes in the body.[4,8] BSA stands out as a robust protein model due to its intrinsic resemblance to HSA and several practical advantages such as affordability, widespread availability, and a pronounced ability to bind to various ligands.[9,10] The interaction between metal complexes and these proteins profoundly influences the distribution of metal complexes or drugs across bodily systems, their therapeutic efficacy, and their metabolic fate, in addition to controlling their engagement with specific target tissues.[11]

Luminescent transition metal complexes, particularly those featuring a d^6 electronic configuration such as Ru(II), Os(II), and Re(I), have garnered substantial research interest as prominent candidates in the domain of biomolecule imaging and

[a]*Department of Chemistry, Indian Institute of Technology Palakkad, Palakkad-678557, Kerala, India. E-mail: shanmugam@iitpkd.ac.in*
[b]*Department of Physics, Indian Institute of Technology Palakkad, Palakkad-678557, Kerala, India*
[c]*Department of Biological Sciences and Engineering, Indian Institute of Technology Palakkad, Palakkad-678557, Kerala, India*

†Electronic supplementary information (ESI) available: ESI-MS, ^{1}H &^{13}C NMR, FT-IR, UV-visible absorption, fluorescence titration studies and cell-viability data are available. See DOI: https://doi.org/10.1039/d5dt00769k

luminescent probes.[12] Within this category, Ru(II) complexes bound to heterocyclic N-donor ligands have been widely examined owing to their interesting optical properties, such as encompassing a broad absorption spectrum emanating from metal-to-ligand charge transfer (MLCT), coupled with well-matched energy levels for both excited and ground states.[13] These complexes exhibit remarkable luminescence quantum yields, robust structural stability, and extended excited state lifetimes under photochemical and electrochemical conditions.[14] The significance of Ru(II) metal complexes extends across various applications. Noteworthy among them are their critical roles as key constituents in the construction of solar energy conversion devices, the illumination of light-emitting diodes (LEDs), and their utility as dye-sensitised photoelectrochemical cells, molecular probes, non-linear optical (NLO) materials, and potent photocatalysts.[15–21] On top of all these, Ru(II) metal complexes are extensively used in the field of cancer therapy because of their platinum-like ligand exchange kinetics, ability to imitate the binding nature of iron with various serum albumin proteins in the plasma, and less toxic nature.[21,22] Among different techniques, fluorescence-based sensing has emerged as an attractive method for studying the binding affinity of metal complexes with various proteins owing to their swiftness, feasibility, exceptional sensitivity, and selectivity.

In the past, the binding properties of transition metal complexes towards biomolecules, particularly for DNA and proteins, have been actively pursued.[22,23] In this regard, Ru(II)/Ru(III)-based metal complexes have shown great promise as potential protein-binding agents. Half-sandwich Ru(II)–arene complexes received special attention due to their facile ligand exchange kinetics, structure, and functional tunability to target specific proteins. There are early reports on half-sandwich Ru(II)–arene complexes-based fluorescence probes with a preferential binding affinity towards serum albumins.[24–26] previous studies have shown that the binding affinity of Ru(II)–metal complexes towards serum proteins depends on several factors, including size, shape, charge, hydrophobicity, and coordination geometry of metal complexes.[25] Also, the functionality of ligands bound to the metal complexes plays an important role in the specific interactions (*i.e.*, hydrogen bonding, π–π stacking, van der Waals forces and so on) of metal complexes with proteins.[23,26] Therefore, the binding of metal complexes towards serum proteins can be improved by selecting suitable metal complexes adorned with desired functional moieties. Early reports have demonstrated that half-sandwich Ru(II)–arene complexes based on poly-pyridyl and π-conjugated ligands exhibit enhanced, preferential binding propensity towards BSA and HSA proteins.[23–26] Based on these early studies, we report three new *p*-cymene–Ru(II) organometallic complexes based on structurally unique 4-amino-1,8-naphthalimide Tröger's bases (**TBNaps**) scaffolds.

TBNaps are a prominent class of cleft-shaped C_2-symmetric fluorescent scaffolds, strongly coloured and highly emissive, attributed to their distinctive 'push-pull' type internal-charge transfer (ICT) transitions.[27–30] Through a dedicated effort in the recent past, we have successfully synthesised a plethora of **TBNap** derivatives and employed them as bifunctional scaffolds to generate multifunctional supramolecular structures and luminescent organic/inorganic polymers for meaningful applications spanning from biomedicine, and chemosensing, to environmental sciences.[29,30] These **TBNaps** exhibit excellent biological properties such as fast and effective cellular internalisation,[31] substantial DNA binding,[32] and cellular apoptosis in certain cancerous cell lines.[33,34] In addition, the fluorescence capabilities of these structures have also been exploited, enabling their role as sensitive fluorescence sensors for the trace detection of secondary chemical explosives, volatile organic compounds, and analytes of vital biological importance.[29,30,35] We have recently shown that conjugation of **TBNap** scaffolds with *p*-cymene–Ru(II)–curcumin complexes resulted in the generation of multifunctional organometallic conjugates with excellent functional properties and exploited them as theragnostic agents against different cancer cell lines.[27,34,36]

Given the advancements of **TBNaps** in cancer studies and the continuation of our earlier reports, herein, we report three new **TBNap**-based *p*-cymene Ru(II) organometallic conjugates (**TB-Ru-1**, **TB-Ru-2**, and **TB-Ru-3**) and their photophysics, bioimaging, and cytotoxicity, as well as BSA/HSA binding properties. The conjugates were obtained by reacting three different **TBNap**-based dipyridyl donors (**TBNap-1**, **TBNap-2**, and **TBNap-3**) separately with dichloro(*p*-cymene)ruthenium(II) dimer (see Scheme 1 for the structures). These conjugates were characterised by NMR (^{1}H and ^{13}C), ESI-MS, and FT-IR analyses. The energy-minimised structure of conjugates was obtained by computational optimisation. Given the multifunctional characteristics and structural uniqueness, we anticipated that the newly designed conjugates **TB-Ru-1**, **TB-Ru-2**, and **TB-Ru-3** could exhibit strong binding affinity towards BSA/HSA proteins. The large hydrophobic cavity in **TBNap** can facilitate the strong hydrophobic interactions with Sudlow sites I & II, two major binding sites, of HSA/BSA proteins.[24] Also, the planar structure of 1,8-naphthalimide may be involved in strong π–π stacking interactions with tryptophan (Trp), tyrosine (Tyr), and phenylalanine (Phe) amino acid residues of serum proteins, which can result in aggregation-caused changes in fluorescence emission intensity of conjugates.[31] The Tröger's base two stereogenic 'N' atoms may form intermolecular hydrogen bonding with the protein backbone.[29] Similarly, Ru(II) can coordinatively interact with side-chain amino-acid residues of proteins.[25] All these properties motivated us to explore the binding properties of all three conjugates towards BSA/HSA proteins. Indeed, the UV-visible absorption and fluorescence emission titration studies showed a strong binding affinity between conjugates **TBNap-1**, **TBNap-2**, and **TBNap-3** and BSA/HSA serum proteins. Besides, these conjugates exhibited a fast-cellular internalisation within a normal 3T3 mouse fibroblast cell line as examined using confocal microscopy. The MTT cell viability assay affirms the biocompatibility and non-toxic nature of the conjugates towards both normal and cancer cell lines.

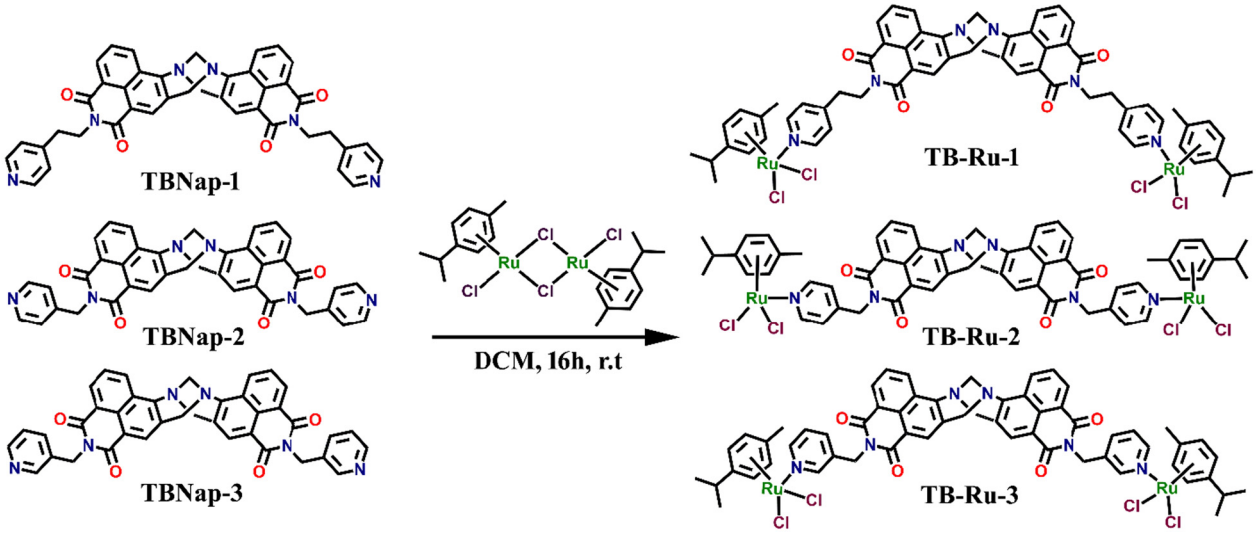

Scheme 1 One-step synthesis of organometallic conjugates **TB-Ru-1**, **TB-Ru-2**, and **TB-Ru-3** from their corresponding dipyridyl donor **TBNap-1**, **TBNap-2**, and **TBNap-3**, respectively.

Experimental

Materials and methods

All the chemicals and reagents were purchased from Sigma-Aldrich and used as received without any purification. The solvents were of HPLC grade and were purchased from reliable vendors. Deuterated solvent $CDCl_3$ used for NMR analyses was purchased from Sigma-Aldrich. The precursors 4-nitro-1,8-naphthalic anhydride, 4-(aminomethyl)pyridine, 3-(aminomethyl)pyridine, 4-(2-aminoethyl)pyridine and dichloro(*p*-cymene)ruthenium(II)dimer were purchased from Sigma-Aldrich and were used as received. The **TBNap**-based dipyridyl donors, Bis-[*N*-(4-(pyridyl)ethyl)]-9,18-methano-1,8-naphthalimide-[*b*,*f*][1,5]diazocine (**TBNap-1**),[37] Bis-[*N*-(4-(pyridyl)methyl)]-9,18-methano-1,8-naphthalimide-[*b*,*f*][1,5]diazocine (**TBNap-2**),[30] and Bis-[*N*-(3-(pyridyl)methyl)]-9,18-methano-1,8-naphthalimide-[*b*,*f*][1,5]diazocine (**TBNap-3**)[38] were synthesised following the procedure reported in the literature.

The melting point of the conjugate was identified using an Electrochemical IA9000 digital melting point apparatus. The elemental analysis of conjugates was performed using a CHN–O analyser available at GSCoE, IIT Palakkad. The ATR sampler-equipped Shimadzu Scientific Instruments (IR Tracer 100) was employed to record FT-IR spectra of conjugates. A Bruker high-performance digital FT-NMR spectrometer functioning at 500 MHz was used to analyse the ^{1}H and ^{13}C NMR spectra. All NMR spectra were recorded in $CDCl_3$ and the spectra were properly comprehended using MestReNova supporting software. The mass of the complexes was analysed using a Micromass LCT spectrometer or a MALDI Q-ToF Premier employing the electron spray ionisation method in positive and negative modes. HPLC-grade CH_3OH was used as the carrier solvent. UV-visible absorption spectra were recorded in 1 cm quartz cuvettes on a Thermo Scientific Evolution 201 spectrometer. Baseline correction was applied for all measurements. The fluorescence emission spectra were recorded on the PerkinElmer-6500 Fluorimeter. All the measurements were carried out at 298 K, and spectral data were analysed and plotted using OriginPro 8.5.

General procedure for the synthesis of organometallic conjugates

In a glass vial, a mixture of dichloro(*p*-cymene)ruthenium(II) dimer ($[Ru(p\text{-cymene})Cl_2]_2$, 1.0 equiv.) and **TBNap** dipyridyl donor (1.0 equiv.) was stirred in DCM (5 mL) for 16 h at room temperature. The solution was filtered, and the clear reddish-orange filtrate was dried under a vacuum. The conjugates were isolated as a reddish-orange powder after trituration with cold diethyl ether.

TB-Ru-1. The product was isolated by reacting dichloro(*p*-cymene)ruthenium(II) dimer (9.2 mg, 0.015 mmol, 1.0 equiv.) and **TBNap-1** (10 mg, 0.015 mmol, 1.0 equiv.). Isolated yield = 63%. Melting point = >200 °C (decomp.). Anal. calcd (%) for $C_{61}H_{58}Cl_4N_6O_4Ru_2{\cdot}3CH_2Cl_2$: C, 50.0; H, 4.2; N, 5.4. Found: C, 50.5; H, 4.4; N, 5.5. ESI-MS (*m*/*z*): Calculated 1248.1750 $[M - Cl + H]^+$, Found 1248.1629; ^{1}H NMR (500 MHz, CD_3Cl) δ 8.85–8.83 (4H, d, J = 10 Hz, $H_{pyridyl}$), 8.70–8.69 (2H, d, J = 5 Hz, H_{Nap}), 8.53–8.52 (2H, d, J = 5 Hz, H_{Nap}), 8.05 (2H, s, H_{Nap}), 7.87–7.84 (2H, t, J = 10 Hz, H_{Nap}), 7.24–7.22 (4H, d, J = 10 Hz, $H_{pyridyl}$), 5.47–5.46 (2H, d, J = 5 Hz, H_{cymene}), 5.41–5.40 (2H, d, J = 5 Hz, H_{cymene}), 5.21–5.19 (4H, t, J = 5 Hz, H_{cymene}), 5.16–5.13 (2H, d, J = 15 Hz, Tröger's base-CH_2), 4.66 (2H, s, Tröger's base-CH_2), 4.60–4.57 (2H, d, J = 15 Hz, Tröger's base-CH_2), 4.42 (2H, m, ethyl-CH_2), 4.37 (2H, m, ethyl-CH_2), 3.08–3.04 (4H, m, ethyl-CH_2), 2.94 (2H, septet, $CH(CH_3)_2$), 2.01 (6H, s, cymene-CH_3), 1.30–1.28 (12H, d, J = 10 Hz, cymene-$CH(CH_3)_2$) ppm; ^{13}C NMR (126 MHz, $CDCl_3$) δ 164.0, 163.4, 154.4, 149.9, 149.5, 131.1, 131.0, 129.2, 128.3, 127.4, 127.1, 125.4,

125.3, 122.7, 118.3, 103.3, 97.1, 83.0, 82.9, 82.1, 57.1, 39.8, 33.2, 30.6, 22.3, 22.3, 18.2 ppm; FT-IR ν_{max} (ATR, cm^{-1}) 3472, 3071, 2955, 1697, 1651, 1597, 1504, 1458, 1381, 1342, 1304, 1258, 1150, 1126, 1057, 1026, 918, 871, 787, 687, 664, 579, 501, 440.

TB-Ru-2. The product was isolated by reacting dichloro(*p*-cymene)ruthenium(II) dimer (9.6 mg, 0.016 mmol, 1.0 equiv.) and **TBNap-2** (10 mg, 0.016 mmol, 1.0 equiv.). Isolated yield = 61%. Melting point = >200 °C (decomp.). Anal. calcd (%) for $C_{59}H_{54}Cl_4N_6O_4Ru_2{\cdot}5CH_2Cl_2$: C, 45.6; H, 3.8; N, 5.0. Found: C, 45.4; H, 3.8; N, 4.9. ESI-MS (*m*/*z*): Calculated 1220.1437 $[M - Cl + H]^+$, Found 1220.1326. ^1H NMR (500 MHz, CD_3Cl) δ 8.87–8.86 (4H, d, J = 5 Hz, $H_{pyridyl}$), 8.71–8.70 (2H, d, J = 5 Hz, H_{Nap}), 8.57–8.56 (2H, d, J = 5 Hz, H_{Nap}), 8.07 (2H, s, H_{Nap}), 7.88–7.85 (2H, t, J = 15 Hz, H_{Nap}), 7.32–7.31 (4H, d, J = 5 Hz, $H_{pyridyl}$), 5.40–5.39 (4H, d, J = 5 Hz, H_{cymene}), 5.30 (4H, s, CH_2-H_{Nap}), 5.19–5.18 (4H, d, J = 5 Hz, H_{cymene}), 5.17–5.14 (2H, d, J = 15 Hz, Tröger's base-CH_2), 4.68 (2H, s, Tröger's base-CH_2), 4.58–4.55 (2H, d, J = 15 Hz, Tröger's base-CH_2), 2.95 (2H, septet, $CH(CH_3)_2$), 2.04 (6H, s, cymene-CH_3), 1.27–1.26 (12H, d, J = 5 Hz, cymene-$CH(CH_3)_2$); ^{13}C NMR (126 MHz, $CDCl_3$) δ 163.9, 163.3, 154.7, 149.8, 148.2, 131.5, 131.1, 129.5, 128.4, 127.4, 127.3, 125.5, 124.2, 122.5, 118.2, 103.6, 96.9, 82.6, 82.3, 82.3, 67.0, 57.3, 41.9, 31.0, 22.3, 18.2; FT-IR ν_{max} (ATR, cm^{-1}) 3471, 3063, 2963, 1697, 1659, 1597, 1497, 1458, 1373, 1342, 1303, 1234, 1322, 1197, 1088, 1057,1026, 964, 917, 864, 787, 756, 686, 664, 617, 579, 517, 447.

TB-Ru-3. The product was isolated by reacting dichloro(*p*-cymene)ruthenium(II) dimer (9.6 mg, 0.016 mmol, 1.0 equiv.) and **TBNap-3** (10 mg, 0.016 mmol, 1.0 equiv.). Isolated yield = 52%. Melting point = >200 °C (decomp.). Anal. calcd (%) for $C_{59}H_{54}Cl_4N_6O_4Ru_2{\cdot}6CH_2Cl_2$: C, 44.2; H, 3.7; N, 4.7. Found: C, 44.3; H, 3.5; N, 4.4. ESI-MS (*m*/*z*): Calculated 1220.1437 $[M - Cl + H]^+$, Found 1220.1293; ^1H NMR (500 MHz, CD_3Cl) δ 9.18 (2H, s, $H_{pyridyl}$), 8.86–8.85 (2H, d, J = 5 Hz, $H_{pyridyl}$), 8.70–8.69 (2H, d, J = 5 Hz, H_{Nap}), 8.59–8.57 (2H, d, J = 10 Hz, H_{Nap}), 8.09 (2H, s, H_{Nap}), 7.88–7.82 (2H, dd, J = 10 Hz, $H_{pyridyl}$), 7.19–7.16 (2H, t, J = 15 Hz, H_{Nap}), 5.40–5.39 (4H, d, J = 5 Hz, H_{cymene}), 5.27 (4H, s, CH_2-H_{Nap}), 5.22–5.21 (4H, d, J = 5 Hz, H_{cymene}), 5.16–5.12 (2H, d, J = 20 Hz, Tröger's base-CH_2), 4.68 (2H, s, Tröger's base-CH_2), 4.57–4.54 (2H, d, J = 15 Hz, Tröger's base-CH_2), 2.95 (2H, septet, $CH(CH_3)_2$), 2.05 (6H, s, cymene-CH_3), 1.27–1.26 (12H, d, J = 5 Hz, cymene-$CH(CH_3)_2$) ppm; ^{13}C NMR (126 MHz, $CDCl_3$) δ 164.0, 163.4, 156.2, 153.5, 149.6, 138.4, 134.0, 131.3, 131.0, 129.2, 128.4, 127.3, 127.2, 125.5, 124.1, 122.8, 118.5, 103.7, 96.8, 82.6, 82.5, 82.4, 67.1, 57.1, 40.6, 30.6, 22.3, 18.1 ppm; FT-IR ν_{max} (ATR, cm^{-1}) 3487, 3063, 2962, 1697, 1651, 1597, 1435, 1404, 1373, 1335, 1304, 1234, 1157, 1111, 1057, 1026, 957, 910, 864, 787, 756, 702, 625, 517, 446.

Fluorescence titration studies using HSA/BSA proteins

In a standard measuring flask, 1 mM stock solutions of **TB-Ru-1**, **TB-Ru-2**, and **TB-Ru-3** were prepared and further diluted to obtain solutions of different concentrations. Similarly, 10 μM concentrations of BSA and HSA were prepared in a phosphate buffer. The excitation wavelength was kept constant at λ = 280 nm, corresponding to the absorption maxima of BSA and HSA. Initially, 2 mL of a 10 μM solution of BSA was taken in a quartz cuvette, and the fluorescence spectra were recorded. To this solution, the stock solution of conjugates (1 to 10 μM) was gradually added. After each addition, the fluorescence emission spectra were recorded at room temperature. A similar titration study was carried out with HSA. The fluorescence quenching constant was calculated using the following Stern–Volmer equation:

$$(I_0/I) = 1 + K_{SV}[Q]$$

where I_0 is the initial emission intensity of BSA/HSA protein in the absence of conjugates; I is the fluorescence emission in the presence of a different concentration of conjugates; [Q] is the molar concentration of conjugates, and K_{SV} is the Stern–Volmer quenching constant.

Biological studies

Cell viability. 3T3 (normal mouse fibroblast) cells were used for viability and internalisation studies. The cells were cultured in Dulbecco's Modified Eagle's medium (DMEM) high glucose media (Himedia) with 10% Fetal bovine serum (FBS) (Himedia) and 1% Penstrep and 0.2% of Amphotericin (Gibco Life Tech). 1% antibiotic at 37 °C and 5% CO_2.

Viability assay. For the viability study, the cells were seeded in 96-well plates with 1×10^4 cells per well. They were allowed to adhere to the substrate overnight in a CO_2 incubator. Cells were incubated for 24 h with various concentrations (1 to 100 μM) of **TB-Ru-1**, **TB-Ru-2**, and **TB-Ru-3**. Post-incubation, 10 μL of MTT was added to each well with a final concentration of 0.5 mg mL^{-1}. The formazan crystals formed were dissolved in DMSO, and absorbance was recorded in a plate reader (Biotech Epoch 2NS Gen5) at λ = 590 nm. Absorbance was also recorded using a λ = 620 nm filter as a reference. Viability data were normalised with the absorbance recorded from an untreated control sample. The data were plotted as a percentage of viability, with standard error obtained from measuring three wells.

Epi-fluorescence microscopy. The cells were seeded on glass coverslips for the internalisation study. After adhesion to the substrate, cells were incubated with the conjugates for 12 h at a concentration of 20 μM for each sample. Post-incubation, cells were fixed using paraformaldehyde, and imaging was done using an *epi*-fluorescence microscope (Olympus IX83) using appropriate excitation and emission filters. Both phase contrast and fluorescence images of the cells were recorded.

Results and discussion

Synthesis, characterisation, and photophysics of organometallic conjugates

The dipyridyl donors **TBNap-1**, **TBNap-2**, and **TBNap-3** were freshly synthesised using their corresponding amine derivatives, following the procedure outlined in our recent publications.[30,37,38] The three new Ru(II)–organometallic conju-

gates **TB-Ru-1**, **TB-Ru-2**, and **TB-Ru-3** were synthesised in a single step by stirring dichloro(*p*-cymene)ruthenium(II) dimer ([Ru(*p*-cymene)Cl_2]$_2$) and corresponding dipyridyl donor (**TBNap-1** for **TB-Ru-1**, **TBNap-2** for **TB-Ru-2**, and **TBNap-3** for **TB-Ru-3**) in a 1 : 1 stoichiometry ratio in DCM. The solvent was stripped off after 16 h of stirring at room temperature (Scheme 1). Trituration with cold diethyl ether yielded the expected conjugates as a reddish-orange powder in analytically pure form (for more details, see the Experimental section). The conjugates were stable in open-air conditions and well soluble in common organic solvents like $CHCl_3$, CH_2Cl_2, CH_3CN, CH_3OH, DMSO, *etc*. The conjugates were then characterised using ESI-MS, multinuclear NMR (^{1}H and ^{13}C), and FT-IR analyses. The ESI-MS analysis of conjugates showed a sharp peak at *m*/*z* = 1248.1629 for **TB-Ru-1**, 1220.1326 for **TB-Ru-2**, and 1220.1293 for **TB-Ru-3**, corresponding to the fragment $[M - Cl + H]^+$ (see Fig. 1 and Fig. S1, S2 in ESI†). These peaks were isotopically well-resolved and matched with the theoretically predicted isotopic patterns.

The ^{1}H NMR spectra of the conjugates exhibit proton resonances as two doublets and a singlet in the range of 5.16–4.57 ppm (for **TB-Ru-1**) (see Fig. 2), 5.17–4.55 ppm (for **TB-Ru-2**), and 5.16–4.54 ppm (for **TB-Ru-3**), corresponding to the Tröger's base moiety (see Fig. S5 and S8 in ESI†). The peaks corresponding to 1,8-naphthalimide appeared as two doublets (8.70–8.69 and 8.59–8.52 ppm), a singlet (8.05–8.09 ppm), and a triplet (7.88–7.16 ppm). The aryl proton signals of capping *p*-cymene appeared as intense doublets in the range of 5.47–5.46 and 5.19–5.18 ppm. Notably, in all the cases, the proton resonances of pyridyl donors were significantly down-field shifted compared to the free **TBNap** dipyridyl donor ligands;[27,31,33–36] it's due to the donation of electron density from ligand-to-metal coordination N: → Ru(II) (see Fig. 2 and ESI Fig. S5, S8†).

The ^{13}C NMR spectra showed sharp resonances corresponding to respective functional moieties of conjugates (Fig. S3, S6, and S9 in ESI†). The FT-IR spectra of conjugates showed a sharp intense band at 1697 cm^{-1} corresponding to the C═O stretching frequency for all three conjugates (Fig. S4, S7, and S10 in ESI†).

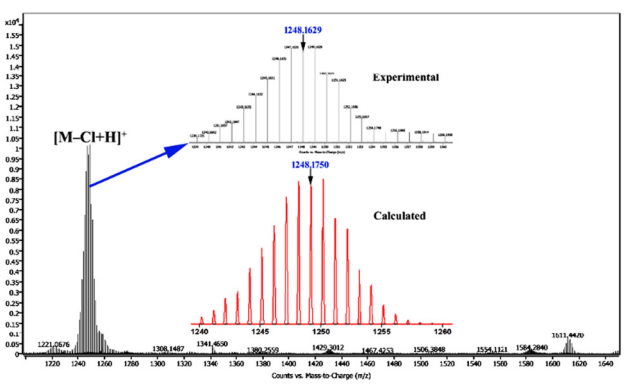

Fig. 1 ESI-MS spectrum of **TB-Ru-1** (inset: the experimental and calculated isotopic distribution of the $[M - Cl + H]^+$ fragment).

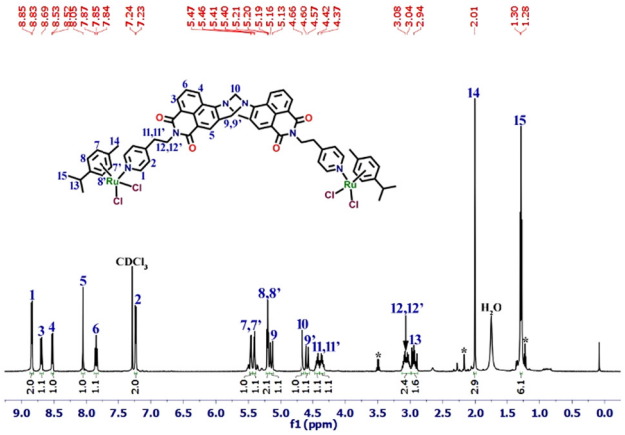

Fig. 2 ^{1}H NMR spectrum of **TB-Ru-1** was recorded in $CDCl_3$ (500 MHz) with peak assignment. *Due to diethyl ether and acetone solvents.

All attempts to obtain single crystals of the conjugates suitable for X-ray diffraction analysis were unsuccessful. Therefore, further structural information was gained by obtaining the energy-minimised structures through molecular mechanics universal force field simulation (MMUFF).[39] As shown in Fig. 3, the optimised structure of conjugates adopts a cleft-shaped conformation, and due to the methano-1,5-diazocine moiety, 1,8-naphthalimide units are close to orthogonal to each other with the mean interplanar angle of 90.68° (**TB-Ru-1**), 84.15° (**TB-Ru-2**), and 86.42° (**TB-Ru-3**). The pyridyl donor moieties in **TB-Ru-2** and **TB-Ru-3** are flanked outwards from

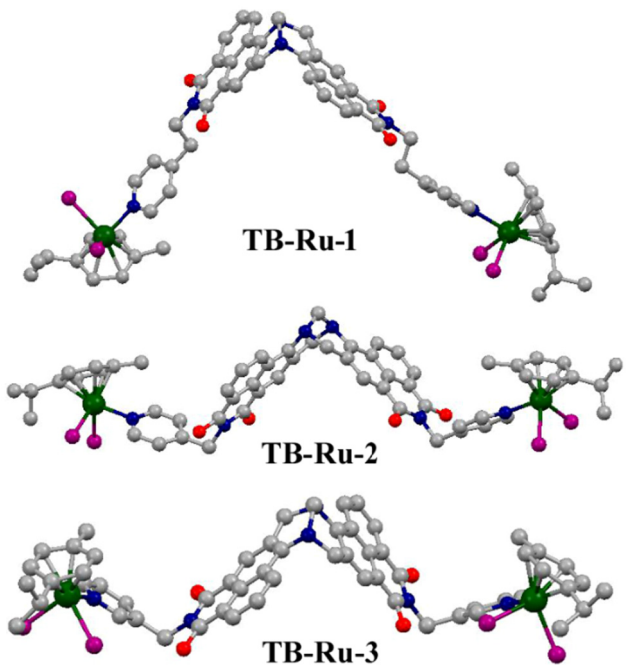

Fig. 3 Optimised structure of conjugates (colour code: C = Gray; O = Red; N = Blue; Ru = Green; Cl = Purple). Hydrogen atoms are excluded for clarity.

the V-shaped cavity. Each Ru(II) centre adopts a three-legged quasi-octahedral (piano-stool) conformation in which three coordination sites are occupied by a *p*-cymene ligand and the other three sites are occupied by coordinated $N_{pyridyl}$ and two Cl^- atoms.

Having synthesised in analytically pure form, we next assessed the UV-visible absorption and fluorescence emission properties of newly synthesised conjugates **TB-Ru-1**, **TB-Ru-2**, and **TB-Ru-3** in a CH_3CN-PBS buffer medium at room temperature. The photophysical studies were performed using 1.0 μM concentrations of conjugates. The electronic absorption spectra of conjugates showed three typical absorption maximum bands in the range λ = 234 to 393 nm (Fig. 4A). The high-energy intense band at λ = 234 to 238 nm corresponds to the π–π* transition, and the low-energy broadband at λ = 388 to 393 nm is ascribed to the internal charge transfer transition (ICT) from the electron-rich Tröger's base to electron-deficient imide sites. The band at λ = 344 to 345 is assigned to the MLCT transition.[13,31] Upon photoexcitation, the conjugates showed an ICT-based strong fluorescence emission band at λ = 496 to 500 nm (Fig. 4B). These ICT bands are slightly red-shifted compared to their respective dipyridyl donors due to metal–ligand coordination bonding.[30,37,38] Furthermore, it was observed that the fluorescence emission intensity of the conjugates was much lower than that of their corresponding TBNap-based dipyridyl donors, possibly due to the excited energy transfer process.[31,36] The fluorescence quantum yield for the conjugates was determined to be φ= 0.05 (for **TB-Ru-1**), 0.04 (for **TB-Ru-2**), and 0.10 (for **TB-Ru-3**). The calculated quantum yield of conjugates is lower than their corresponding **TBNap** donors, and this is attributed to the poor emission of conjugates in solution. Furthermore, the time-dependent UV-visible absorption and fluorescence emission studies using **TB-Ru-2** showed no significant changes in intensity, demonstrating the high stability of newly designed conjugates in solution (Fig. S15, ESI†).

BSA/HSA proteins binding studies

The binding propensity of conjugates toward the serum proteins was assessed by UV-visible absorption and fluorescence emission titration studies in a PBS buffer medium (pH = 7.4). The absorption spectrum of BSA showed a prominent band at λ = 210 nm, which is attributed to the conformation of the protein framework and the peptide bonds, and a less intense peak at λ = 278 nm corresponds to the π–π* transition of aromatic amino acids like tryptophan, phenylalanine, and tyrosine present within the protein chains (Fig. 5A blue line).[10] To corroborate interactions between the conjugates and BSA, the absorption spectrum of BSA was measured before and after the addition of conjugate solutions. In all the cases, the absorption intensity of BSA was increased significantly upon the addition of increasing concentrations of conjugates (Fig. 5A red line and Fig. S11A, S12A†). Along with the hyperchromicity, a clear bathochromic shift in the absorption spectra was observed in all the cases. The increased absorption intensity demonstrates a ground-state charge-transfer complexation between BSA and organometallic conjugates.

The association constant (K_a) was quantitatively evaluated using the following Benesi–Hildebrand equation:[40]

$$1/[A - A_0] = 1/(A_1A_0) + 1/(A_1 - A_0)K_a[Q]$$

where A indicates the absorbance of BSA in the presence of varying concentrations of conjugate; A_0 is the absorbance of BSA in the absence of conjugates, A_1 is the absorbance of the BSA-conjugate, K_a is the association constant derived from the intercept-to-slope ratio, and [Q] denotes the concentrations of the conjugate.

The double reciprocal plot of $1/(A - A_0)$ *vs.* 1/[conjugates] displayed linearity, which indicates a 1 : 1 ground-state complex formation between BSA and conjugates (Fig. 5B and Fig. S11B, 12B†). From the slope of the linear curve, the association constant K_a was determined to be 5.89×10^4 M^{-1} (for **TB-Ru-1**), 3.87×10^4 M^{-1} (for **TB-Ru-2**), and 5.09×10^4 M^{-1} (for **TB-Ru-3**).[41,42] Under the same experimental conditions, similar absorption titration studies were performed using HSA protein. After conjugates were added in increasing concentration, the absorption intensity of HSA was increased signifi-

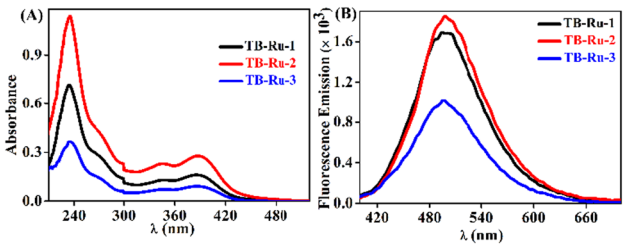

Fig. 4 (A) UV-visible absorption and (B) fluorescence emission spectra of conjugates (1.0 μM) measured in CH_3CN-PBS buffer medium at room temperature.

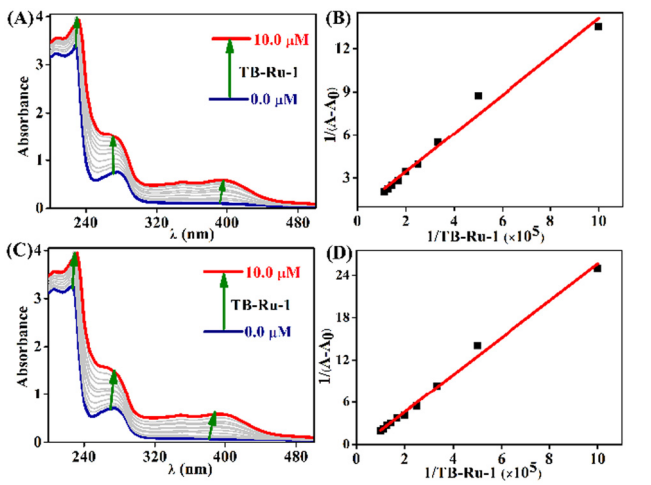

Fig. 5 The observed changes in UV-visible absorption spectra of (A) BSA and (C) HSA proteins after the gradual addition of **TB-Ru-1** in increasing concentration (1 to 10 μM) measured in PBS buffer medium at room temperature and their corresponding Benesi–Hildebrand plot (B and D).

cantly, accompanied by a notable bathochromic shift (Fig. 5C, D and Fig. S11C, D, S12C, D†). K_a was determined to be 2.29 × 10^4 M^{-1} (for **TB-Ru-1**), 8.78 × 10^3 M^{-1} (for **TB-Ru-2**), and 4.68 × 10^3 M^{-1} (for **TB-Ru-3**). The intrinsic fluorescence of BSA predominantly arises from the presence of two Trp residues located at positions 134 and 212 in domains IB and IIA, respectively. Alterations in the emission maxima or intensity directly signify changes in the surrounding polarity near these Trp residues, indicative of a shift from the native conformation. Therefore, monitoring the intrinsic fluorescence of BSA serves as a valuable means to track the binding of **TBNap** conjugates to BSA.

We performed fluorescence titration studies to probe the binding between conjugates and proteins. For this, a 10 μM PBS buffer solution of BSA was initially taken in the quartz cuvette, and the emission spectrum was recorded. Upon excitation at λ = 280 nm, BSA showed a strong fluorescence emission maximum at λ = 350 nm assigned to the intrinsic fluorescence of BSA arising from Trp and Tyr units. To this BSA solution, a freshly prepared stock solution of conjugates (1 to 10 μM) was added separately, and the emission spectra were recorded after each addition. We observed significant fluorescence quenching following the addition of each conjugate. This was accompanied by a slight blue shift in the emission maxima for all three conjugates (Fig. 6A and Fig. S13A, 14A†). This result confirms the interaction between the conjugates and BSA (Trp-212, emission at λ = 340 nm), leading to the formation of non-fluorescent complexes. Notably, the blue shift suggests that the interactions between BSA and the conjugates are primarily hydrophobic in nature. A similar fluorescence quenching pattern was observed upon adding the conjugates to the HSA solution (Fig. 6C and Fig. S13C, 14C†). The conjugates strongly bind to Trp-214, with the emission maximum at λ = 340 nm. From the titration profiles, the Stern–Volmer quenching constant (K_{SV}) was calculated for all conjugates with BSA and HSA. The determined K_{SV} values for BSA are 7.97 × 10^4 M^{-1} (for **TB-Ru-1**), 1.26 × 10^5 M^{-1} (for **TB-Ru-2**), and 1.03 × 10^5 M^{-1} (for **TB-Ru-3**). Similarly, the calculated K_{SV} values for HSA are 1.31 × 10^5 M^{-1} (for **TB-Ru-1**), 9.97 × 10^4 M^{-1} (for **TB-Ru-2**), and 1.34 × 10^5 M^{-1} (for **TB-Ru-3**). The high K_{SV} values indicate stronger binding between the serum proteins and the conjugates. Furthermore, the higher K_{SV} values suggest that the conjugates **TB-Ru-1** and **TB-Ru-2** may induce structural changes. Thus, there can be rearrangements in the BSA and HSA proteins near their respective binding sites. The conjugate **TB-Ru-3** binding affinity toward both proteins was weak, possibly due to the orientation of the 3-pyridyl nitrogen, which may not position the metal ions favourably for interaction with the protein binding sites.

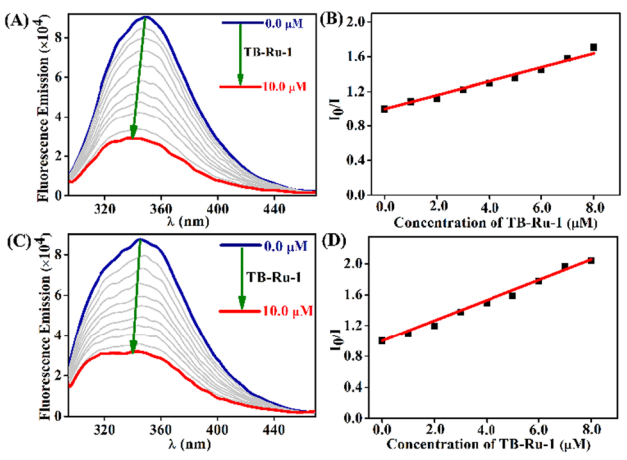

Fig. 6 The fluorescence emission spectra of (A) BSA and (C) HSA before and after the gradual addition of increasing concentrations of conjugate **TB-Ru-1** (1 to 10 μM) measured in PBS buffer medium at room temperature and their corresponding Stern–Volmer plot (B and D).

Biological studies

We then studied the biological properties of conjugates. The cellular internalisation of three conjugates within 3T3 (normal mouse fibroblast) cell lines was probed using confocal laser scanning microscopy. The 3T3 cell lines were incubated with three conjugates separately for 24 h and the fluorescence microscopy images were recorded. **TB-Ru-3** was found to form large aggregates at the cell membranes. So, no confocal fluorescence images and cell viability assays were collected for **TB-Ru-3**. **TB-Ru-1** and **TB-Ru-2** were internalised quickly within 3T3 cell lines and localised within the cytoplasm or on the edges of the nucleus (see Fig. 7). The observed bright green emissions emanating from the internalised conjugates.

The cytotoxicity of **TB-Ru-1** and **TB-Ru-2** against 3T3 cell lines was assessed using the MTT assay, which measures cell viability based on the conversion of MTT to formazan. The bar graph plotting the percentage (%) of cell viability *vs* concentration is shown in Fig. 8 and summarised in Table S1 in ESI.† The estimated IC_{50} values from the MTT assay confirmed that **TB-Ru-1** and **TB-Ru-2** were bio-compatible, and no substantial toxicity was observed even after 24 hours of incubation at different concentrations of conjugates against the 3T3 cell line. These results demonstrate the non-toxic nature of newly designed conjugates against healthy cells. These findings suggest that the conjugates **TB-Ru-1** and **TB-Ru-2** may hold promise as potential candidates for biomedical applications.

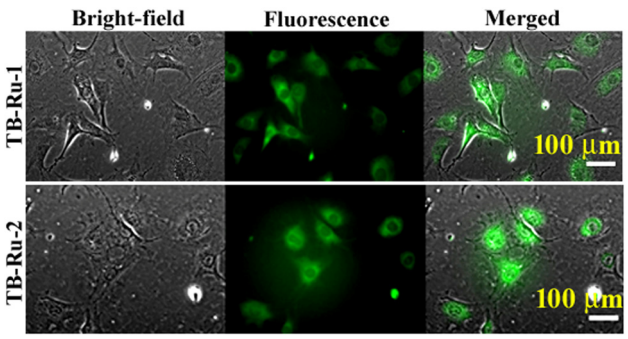

Fig. 7 Confocal live-cell images of **TB-Ru-1** (20 μM) and **TB-Ru-2** (20 μM) after 12 h of incubation within 3T3 (normal mouse fibroblast) cells.

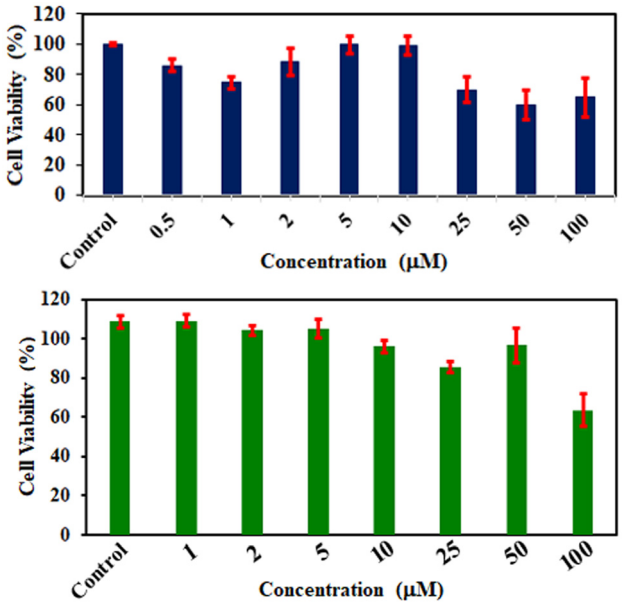

Fig. 8 Cell viability profile of **TB-Ru-1** (above) and **TB-Ru-2** (below) in 3T3 (normal mouse fibroblast) cells after 24 h with varied concentrations (1 to 100 μM).

Conclusions

In summary, we have successfully designed and synthesised three new *p*-cymene-Ru(II) organometallic conjugates, **TB-Ru-1**, **TB-Ru-2**, and **TB-Ru-3**, based on green-fluorescent **TBNap**-based dipyridyl donors (**TBNap-1**, **TBNap-2**, and **TBNap-3**). The photophysical properties of conjugates were measured, and their binding properties with BSA and HSA were assessed, aiming to facilitate the rational design of metallodrugs for biomedical purposes. Furthermore, the conjugates exhibited rapid cellular uptake and displayed a strong green fluorescence emission within the 3T3 normal mouse fibroblast cell lines, thus demonstrating their use as cellular imaging probes. The non-toxic and biocompatible nature of conjugates enhances their practical use in cellular environments. This study underscores the potential of **TBNap** scaffolds as promising ligands for the development of potential metallodrugs. Further work is in progress to modify the TBNap-based metal complexes, aiming to enhance their anticancer properties by incorporating various bioactive ligands.

Author contributions

Binduja Mohan: data curation, formal analysis, investigation, methodology, writing – original draft; Anna Jose: data curation, formal analysis, investigation; Indrajit Bhattacharjee: data curation, formal analysis, investigation; Saravanan Raju: formal analysis, resources, software, validation; Mannanthara Kunhumon Noushija: formal analysis, resources, software, validation; Mintu Porel: supervision, writing – review & editing; Bibhu Ranjan Sarangi: supervision, writing – review & editing; Sankarasekaran Shanmugaraju: conceptualization, funding acquisition, methodology, project administration, software, supervision, writing – review & editing.

Conflicts of interest

There are no conflicts to declare.

Data availability

The data supporting this article have been included as part of the ESI.† The data can be shared on request to the corresponding author.

Acknowledgements

The authors are thankful to the Indian Institute of Technology Palakkad (ERG research grant 2023-168-CHY–SHS–ERG-SP to S. S.), and the Science and Engineering Research Board (EMEQ research grant EEQ/2023/000386 to S. S.) India for funding support and CIF at the Indian Institute of Technology Palakkad for the research facility.

References

1 H.-H. Han, A. C. Sedgwick, Y. Shang, N. Li, T. Liu, B.-H. Li, K. Yu, Y. Zang, J. T. Brewster, M. L. Odyniec, M. Weber, S. D. Bull, J. Li, J. L. Sessler, T. D. James, X.-P. He and H. Tian, *Chem. Sci.*, 2020, **11**, 1107–1113.
2 A. Anish Babu, K. Karthick, R. Subramanian and K. Swarnalatha, *J. Biomol. Struct. Dyn.*, 2020, **38**, 4032–4039.
3 X. Li and Z. Yang, *Chem.-Biol. Interact.*, 2015, **232**, 77–84.
4 G. Fanali, A. di Masi, V. Trezza, M. Marino, M. Fasano and P. Ascenzi, *Mol. Aspects Med.*, 2012, **33**, 209–290.
5 R. B. Klanderman, J. J. Bosboom, H. Korsten, T. Zeiler, R. E. A. Musson, D. P. Veelo, B. F. Geerts, R. van Bruggen, D. de Korte and A. P. J. Vlaar, *Vox Sang.*, 2020, **115**, 664–675.
6 O. A. Chaves, V. A. da Silva, C. M. R. Sant'Anna, A. B. B. Ferreira, T. A. N. Ribeiro, M. G. de Carvalho, D. Cesarin-Sobrinho and J. C. Netto-Ferreira, *J. Mol. Struct.*, 2017, **1128**, 606–611.
7 N. Zhang, H. He, M. Zhang, X. Lv, W. Li, R. Wang and J. Chang, *New J. Chem.*, 2022, **46**, 12814–12824.
8 Y. Dai, J. Gong, J. Cao, W. Chen and N. Fu, *Dyes Pigm.*, 2024, **222**, 111893.
9 H. Zhou, X. Shi, Y. Fan, Z. He, W. Gu, L. Ye and F. Meng, *J. Biomol. Struct. Dyn.*, 2018, **36**, 254–261.
10 J.-h. Shi, D.-q. Pan, M. Jiang, T.-T. Liu and Q. Wang, *J. Biomol. Struct. Dyn.*, 2017, **35**, 2211–2223.
11 K. Swarnalatha, P. Rathnamala, A. A. Babu and N. Bhuvanesh, *J. Struct. Chem.*, 2016, **57**, 1554–1560.

12 E. Babu, P. Muthu Mareeswaran, S. Singaravadivel, J. Bhuvaneswari and S. Rajagopal, *Spectrochim. Acta, Part A*, 2014, **130**, 553–560.
13 F. E. Poynton, S. A. Bright, S. Blasco, D. C. Williams, J. M. Kelly and T. Gunnlaugsson, *Chem. Soc. Rev.*, 2017, **46**, 7706–7756.
14 F. E. Poynton, J. P. Hall, P. M. Keane, C. Schwarz, I. V. Sazanovich, M. Towrie, T. Gunnlaugsson, C. J. Cardin, D. J. Cardin, S. J. Quinn, C. Long and J. M. Kelly, *Chem. Sci.*, 2016, **7**, 3075–3084; A. A. Ansari, A. K. Parchur and G. Chen, *Coord. Chem. Rev.*, 2022, **457**, 214423.
15 N. Tomar, A. Agrawal, V. S. Dhaka and P. K. Surolia, *Sol. Energy*, 2020, **207**, 59–76.
16 F. G. Gao and A. J. Bard, *J. Am. Chem. Soc.*, 2000, **122**, 7426–7427; S. Swaminathan, J. Haribabu, M. Dharmasivam, N. Maroli, J. P. Jayadharin, N. Balakrishnan, N. Bhuvanesh, C. Echeverria and R. Karvembu, *Inorg. Chem.*, 2023, **62**, 3679–3691.
17 I. Purnama, Salmahaminati, M. Abe, M. Hada, Y. Kubo and J. Y. Mulyana, *Dalton Trans.*, 2019, **48**, 688–695; J. Haribabu, G. Sabapathi, M. M. Tamizh, C. Balachandran, N. S. P. Bhuvanesh, P. Venuvanalingam and R. Karvembu, *Organometallics*, 2018, **37**, 1242–1257.
18 A. N. Boynton, L. Marcélis, A. J. McConnell and J. K. Barton, *Inorg. Chem.*, 2017, **56**, 8381–8389; S. Fulgencio, M. Scaccaglia and A. Frei, *ChemBioChem*, 2024, **25**, e202400435.
19 A. Colombo, C. Dragonetti, D. Marinotto, S. Righetto, G. Griffini, S. Turri, H. Akdas-Kilig, J.-L. Fillaut, A. Amar, A. Boucekkine and C. Katan, *Dalton Trans.*, 2016, **45**, 11052–11060.
20 A. S. Maier, C. Thomas, M. Kränzlein, T. M. Pehl and B. Rieger, *Macromolecules*, 2022, **55**, 7039–7048.
21 G. S. Smith and B. Therrien, *Dalton Trans.*, 2011, **40**, 10793–10800; J. Haribabu, R. Arulkumar, D. Mahendiran, K. Jeyalakshmi, S. Swaminathan, P. Venuvanalingam, N. Bhuvanesh, J. F. Santibanez and R. Karvembu, *Inorg. Chim. Acta*, 2024, **565**, 121973.
22 Q.-X. Zhen, B.-H. Ye, Q.-L. Zhang, J.-G. Liu, L. Hong, L.-N. Ji and L. Wang, *J. Inorg. Biochem.*, 1999, **76**, 47–53.
23 R. K. Vuradi, V. R. Putta, D. Nancherla and S. Sirasani, *J. Fluoresc.*, 2016, **26**, 689–701.
24 S. Opačak, M. P. Kovač, A. Brozovic, I. Piantanida and S. I. Kirin, *Dalton Trans.*, 2023, **52**, 11698–11704.
25 N. K. Singh, Y. Kumar, R. P. Paitandi, R. K. Tiwari, A. Kumar and D. S. Pandey, *Inorg. Chim. Acta*, 2023, **545**, 121241; D. P. Dorairaj, J. Haribabu, M. Dharmasivam, R. E. Malekshah, M. K. M. Subarkhan, C. Echeverria and R. Karvembu, *Inorg. Chem.*, 2023, **62**, 11761–11774.
26 O. Dömötör and É. A. Enyedy, *JBIC, J. Biol. Inorg. Chem.*, 2019, **24**, 703–719.
27 B. Mohan, D. Umadevi and S. Shanmugaraju, *Sens. Diagn.*, 2023, **2**, 262–267.
28 J. M. Delente, D. Umadevi, S. Shanmugaraju, O. Kotova, G. W. Watson and T. Gunnlaugsson, *Chem. Commun.*, 2020, **56**, 2562–2565.
29 S. Shanmugaraju, C. Dabadie, K. Byrne, A. J. Savyasachi, D. Umadevi, W. Schmitt, J. A. Kitchen and T. Gunnlaugsson, *Chem. Sci.*, 2017, **8**, 1535–1546.
30 B. Mohan and S. Shanmugaraju, *Dalton Trans.*, 2023, **52**, 2566–2570.
31 S. A. Bright, M. Erby, F. E. Poynton, D. Monteyne, D. Pérez-Morga, T. Gunnlaugsson, D. C. Williams and R. B. P. Elmes, *RSC Chem. Biol.*, 2024, **5**, 344–359.
32 A. Das, S. Mandal, R. Mukherjee, R. Naskar, N. Murmu and T. K. Mondal, *New J. Chem.*, 2023, **47**, 17359–17372.
33 E. B. Veale and T. Gunnlaugsson, *J. Org. Chem.*, 2010, **75**, 5513–5525.
34 S. Shanmugaraju, B. la Cour Poulsen, T. Arisa, D. Umadevi, H. L. Dalton, C. S. Hawes, S. Estalayo-Adrián, A. J. Savyasachi, G. W. Watson and D. C. Williams, *Chem. Commun.*, 2018, **54**, 4120–4123.
35 J. M. Delente, D. Umadevi, S. Shanmugaraju, O. Kotova, G. W. Watson and T. Gunnlaugsson, *Chem. Commun.*, 2020, **56**, 2562–2565.
36 B. Mohan, S. Estalayo-Adrián, D. Umadevi, B. la Cour Poulsen, S. Blasco, G. J. McManus, T. Gunnlaugsson and S. Shanmugaraju, *Inorg. Chem.*, 2022, **61**, 11592–11599.
37 S. Banerjee, S. A. Bright, J. A. Smith, J. Burgeat, M. Martinez-Calvo, D. C. Williams, J. M. Kelly and T. Gunnlaugsson, *J. Org. Chem.*, 2014, **79**, 9272–9283.
38 S. Shanmugaraju, C. S. Hawes, A. J. Savyasachi, S. Blasco, J. A. Kitchen and T. Gunnlaugsson, *Chem. Commun.*, 2017, **53**, 12512–12515.
39 M. A. Thompson, ; *ArgusLab 4.0*, Planaria Software LLC, Seattle WA, 2004, **https://www.arguslab.com/arguslab.com/Welcome.html**.
40 S. Roy, R. K. Nandi, S. Ganai, K. C. Majumdar and T. K. Das, *J. Pharm. Anal.*, 2017, **7**, 19–26.
41 M. Toprak, *Spectrochim. Acta, Part A*, 2016, **154**, 108–113.
42 L.-L. He, Z.-X. Wang, Y.-X. Wang, X.-P. Liu, Y.-J. Yang, Y.-P. Gao, X. Wang, B. Liu and X. Wang, *Colloids Surf., B*, 2016, **145**, 820–829.